

Particle microphysics and chemistry in remotely observed mountain polar stratospheric clouds

K. S. Carslaw,¹ M. Wirth,² A. Tsias,¹ B. P. Luo,¹ A. Dörnbrack,²
M. Leutbecher,² H. Volkert,² W. Renger,² J. T. Bacmeister,³ and T. Peter¹

Abstract. Polar stratospheric clouds (PSCs) at 22–26 km were observed over the Norwegian mountains by airborne lidar on January 15, 1995. Simulations using a mesoscale model reveal that they were caused by mountain-induced gravity waves. The clouds had a highly detailed filamentary structure with bands as thin as 100 m in the vertical, and moved insignificantly over 4 hours, suggesting them to be quasi-stationary. The aircraft flight path was parallel or close to parallel with the wind at cloud level. Such a quasi-Lagrangian observation, together with the presence of distinct aerosol layers, allows an air parcel trajectory through the cloud to be constructed and enables the lidar images to be simulated using a microphysical box model and light scattering calculations. The results yield detailed information about particle evolution in PSCs and suggest that water ice nucleated directly from liquid $\text{HNO}_3/\text{H}_2\text{SO}_4/\text{H}_2\text{O}$ droplets as much as 4 K below the ice frost point. The observation of solid nitric acid hydrate particles downwind of the mountains shows that such mesoscale events can generate solid PSC particles that can persist on the synoptic scale. We also draw attention to the possible role of mesoscale PSCs in chlorine activation and subsequent ozone destruction.

1. Introduction

Surface-catalysed chemical reactions on polar stratospheric cloud (PSC) particles cause the conversion of relatively inert gaseous chlorine species into photochemically active forms that can lead to the destruction of ozone [World Meteorological Organisation, 1994]. Chlorine activation rates and subsequent ozone destruction increase with decreasing temperature because of the combined increase in particle surface area and the rate coefficients of many surface reactions [Borrmann *et al.*, 1997]. Hence even short-lived small-scale reductions in temperature could lead to efficient chemical processing. In addition to their effect on chemical reaction rates, temperature fluctuations may also be an important means of freezing stratospheric aerosols [Meilinger *et al.*, 1995; Tabazadeh *et al.*, 1996; Tsias *et al.*, 1997], a process which is still poorly understood [Tolbert, 1994; Peter, 1997; Koop *et al.*, 1997a].

An important source of strong temperature fluctuations at stratospheric levels are orographically induced

gravity waves [Nastrom and Fritts, 1992]. Case studies of mountain waves that formed over the Antarctic Peninsula and the Norwegian and Alaskan mountains indicate localized cooling of as much as 5 to 10 K [Gary, 1989; Volkert and Intes, 1992; Dörnbrack *et al.*, 1997; Bacmeister *et al.*, 1994; Peter *et al.*, 1994]. Such events not only have the potential to influence PSC formation [Peter *et al.*, 1992, 1994; Meilinger *et al.*, 1995; Tsias *et al.*, 1997] but could also lead to a dramatic enhancement in the rates of chlorine activation reactions [Carslaw *et al.*, 1998]. The effect of such temperature fluctuations on stratospheric aerosols, PSC formation, and chlorine partitioning depends not only on their frequency of occurrence, but also on parameters such as the depth and period of mountain wave cooling and the associated cooling and heating rates [Tsias *et al.*, 1997]. Until now, no combined measurements of PSC development and mountain wave structure have been available that enable the effect of gravity waves to be explored in detail.

Aircraft observations of PSCs that formed over the Norwegian mountains during January 1995 are described here in detail. An identification of the different particle types in the clouds provides a strong constraint on the local changes in temperature. In addition, the highly resolved aerosol layers apparent in the clouds enable the amplitude and wavelength of the gravity waves to be estimated. By combining results from a microphysical model of the particles with light scattering calculations to simulate the view from the lidar it is pos-

¹Max Planck Institute for Chemistry, Mainz, Germany.

²Deutsche Forschungsanstalt für Luft- und Raumfahrt, Oberpfaffenhofen, Germany.

³Naval Research Laboratory, Washington, D. C.

sible to identify transitions between several PSC types. This leads to a clearer understanding of cloud formation within mountain waves as well as the potential effect of these small-scale features on the stratospheric aerosol as a whole. In the work of *Carshaw et al.* [1998] we use the microphysical results presented here as input to a chemical box model, and show that mesoscale PSCs can cause significant chlorine activation in air parcels flowing over the mountains.

2. Ice Particle Microphysics Determined From Quasi-Lagrangian Cloud Observations

The dual wavelength (354 and 532 nm) Ozone Lidar Experiment lidar [*Wirth and Renger*, 1996] was operated from a Transall aircraft flying at an altitude of 7 km. Flights were made from Kiruna in northern Sweden between December 1994 and April 1995. The PSC observations described here represent a subset of those obtained in the period January 11–17, 1995. They were chosen for closer analysis since the flight path was at times parallel or close to parallel with the wind flow at the level of the PSC, which we term quasi-Lagrangian, and because they appear to show the growth of several different PSC types in close proximity. Plate 1 shows the flight segments described, together with temperatures and horizontal winds on the 560 K potential temperature surface (about 23 km) analyzed by the European Centre for Medium-Range Weather Forecasts (ECMWF).

The lidar instrument has a resolution of 30 m in the vertical and 25 m in the horizontal for an aircraft speed of 125 m s^{-1} relative to the air at the level of the cloud. Three properties of the lidar signal are used to describe the cloud observations; the total backscatter ratio (S) and the backscatter ratio for the perpendicular polarization (S_{\perp}) at 532 nm wavelength, which together enable spherical and nonspherical particles to be distinguished, and the color ratio. In terms of the backscatter coefficient, β , the three optical properties are defined as

$$S = (\beta_{\text{aerosol}} + \beta_{\text{air}}) / \beta_{\text{air}} \quad (1a)$$

$$S_{\perp} = (\beta_{\text{aerosol},\perp} + \beta_{\text{air},\perp}) / \beta_{\text{air},\perp} \quad (1b)$$

$$\text{color ratio} = \beta_{\text{aerosol}}^{354\text{nm}} / \beta_{\text{aerosol}}^{532\text{nm}} \quad (1c)$$

Plates 2a, 2c, and 2e show measurements along part of flight leg 5 with quasi-Lagrangian PSC observations. Quasi-Lagrangian is defined here as an aircraft flight path parallel to the wind at the level of the PSC. The wind direction along leg 5 at 22–24 km was from left to right in Plate 2 and made an angle of less than 3° with the flight path. In order to model the microphysics of this PSC, we assume that it is quasi-stationary; that is, the overall form and position of the wave is assumed not to change significantly during the time required for an air parcel to flow through it, which is about 30 min. Although only a single flight was made below the cloud

in Plate 2, in other cases two passes were made separated by 4 hours (legs 1 and 3 in Plate 1), suggesting quasi-stationarity of the gross cloud features on this timescale. Furthermore, simulations using a mesoscale model, described below, indicate that such waves are probably stationary for at least 1 hour. Although individual cloud particles form and dissipate as they are carried through the cloud with the wind, the cloud itself remains fixed in position by the vertical motion of the air flowing over the mountain.

Two distinct PSC types are apparent within the short flight segment shown in Plate 2. A strongly backscattering banded feature between 30 and 40 km, with a backscatter ratio $S \approx 100$ at 532 nm (Plate 2a) and strong depolarization of the backscattered light (Plate 2e) is indicative of water ice particles [*Toon et al.*, 1990]. The existence of water ice indicates strong localised cooling, since the ice frost point at this altitude is approximately 185.5 K, 8 K lower than the synoptic temperature shown in Plate 1. Such a strong departure in temperature on a scale of ≈ 20 km localized over the mountains strongly suggests that this PSC was induced by mountain waves. The backscatter ratio is typically less than 8 upwind and downwind of the ice PSC, and S_{\perp} is not significantly greater than background levels, which is indicative of type 1b PSCs [*Toon et al.*, 1990]. As we show below, these probably formed from uptake of HNO_3 and H_2O by the background liquid $\text{H}_2\text{SO}_4/\text{H}_2\text{O}$ droplets [*Carshaw et al.*, 1994; *Tabazadeh et al.*, 1994a, b; *Drdla et al.*, 1994; *Carshaw et al.*, 1997].

The fine bands of cloud in Plate 2 have a depth of approximately 100 m and are probably caused by vertical inhomogeneities in the H_2O , HNO_3 , or H_2SO_4 abundance, which would affect both liquid aerosol and ice particle growth and hence the amount of backscattered light. Similar particle microlayers were observed by balloon-borne particle counters over northern Sweden in January 1992 during the European Arctic Stratospheric Ozone Experiment [*Deshler et al.*, 1994].

2.1. Microphysical simulation

The quasi-Lagrangian character of the observations in Plate 2 and the assumption of quasi-stationarity allow the particle microlayers to be considered as “streak lines” of the airflow through the cloud from left to right. The white line in Plates 2a, 2c and 2e represents a likely air parcel trajectory with a temperature shown in Figure 1a. A microphysical simulation was performed along this trajectory, and the modeled particle sizes were used together with a light-scattering algorithm [*Mishchenko*, 1991] to calculate the optical properties S , S_{\perp} , and the color ratio at each position along the white line. Certain quantities in the microphysical model, such as the number density of ice particles, were then adjusted in order to bring the calculated optical properties into agreement with the lidar observations. This process, which enables particle number densities and sizes to be estimated with reasonable accuracy, is

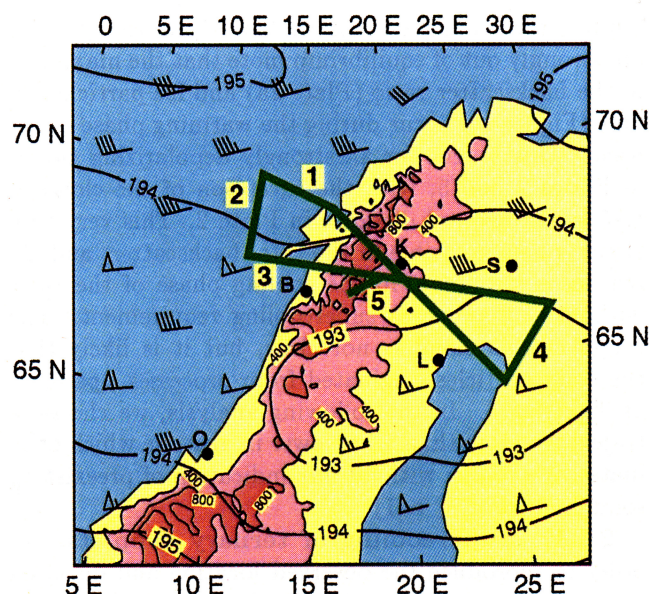


Plate 1. ECMWF-analyzed temperatures (in kelvins) on the 560 K potential temperature surface at 1200 UT on January 15, 1995. The flight legs (green lines) are numbered in the order in which they were flown. The wind field is indicated by flags (short barb, 5 m s^{-1} ; long barb, 10 m s^{-1} ; triangle, 50 m s^{-1}) and significant orography by the red shading, with 400, 800, and 1200 m contours. Locations mentioned in the text are marked by B, Bodø; O, Orland; L, Luleå; K, Kiruna; S, Sodankylä.

described in more detail at appropriate points later in the paper. The calculated optical properties are compared with the observations in Plates 2b, 2d, and 2f.

The microphysical box model is based on that described by Meilinger *et al.* [1995] and calculates the time dependent growth of liquid $\text{HNO}_3/\text{H}_2\text{SO}_4/\text{H}_2\text{O}$ aerosols, and the solid particles nitric acid trihydrate (NAT), nitric acid dihydrate (NAD) and ice, as well as liquid/ice internally mixed particles. A lognormal size distribution of droplet radii is represented by 26 size bins $B_0 - B_{25}$ with a total of $10 \text{ particles cm}^{-3}$, a width of $\sigma = 1.8$ and mode radius of $0.08 \mu\text{m}$ at 230 K. This is equivalent to a total amount of H_2SO_4 in the air parcel of 0.49 ppbv, assumed to be entirely in the condensed phase. Ice and NAT vapor pressures were taken from Hanson and Mauersberger [1988]. To avoid numerical diffusion, particle growth is calculated using a Lagrangian scheme in radial space. The model was initialized with liquid particles, as indicated by the lidar data, with 9 ppbv HNO_3 and 5 ppmv total H_2O .

The determination of the air parcel temperature is rather involved, so it deserves some discussion. The existence of water ice could be used directly to determine the air parcel temperature if the particles were always at equilibrium. This is not the case for the ice particles in Plate 2. However, the frost point level can be calculated with useful accuracy as follows: At the point of maximum backscatter (point 1) the ice particles are

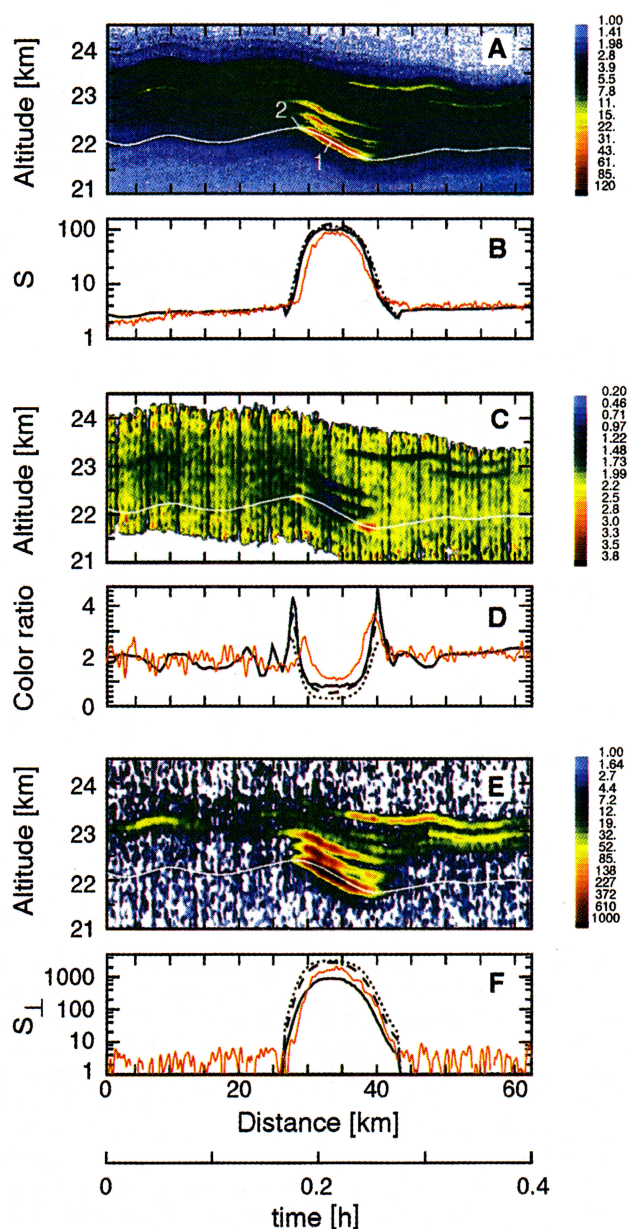


Plate 2. Lidar measurements of January 15, 1995 along flight leg 5. (a) Backscatter ratio at 532 nm laser wavelength, S ; (b) observed S (red line) and calculated S (black line) along white line; (c) color ratio ($\beta_{354\text{nm}}/\beta_{532\text{nm}}$); (d) observed (red) and calculated (black) color ratio along white line; (e) backscatter ratio at 532 nm in perpendicular polarization, S_{\perp} ; (f) observed S_{\perp} (red) and calculated S_{\perp} (black) along white line. The time axis refers to an air parcel flowing through the cloud with a wind speed of 150 km h^{-1} , as determined from ECMWF analyses. Calculations are shown for prolate particles with aspect ratios of 0.85, 0.9, and 0.95 (dotted, dashed, and solid lines, respectively). The optical calculations were made using calculated particle size distributions from the microphysical model simulations (Figure 1) and a light scattering algorithm suitable for non-spherical particles [Mishchenko, 1991]. A refractive index of 1.48 was used for NAT, and 1.31 was used for ice. For liquid aerosols an index of refraction as a function of aerosol composition, temperature and wavelength was used [Krieger *et al.*, 1997].

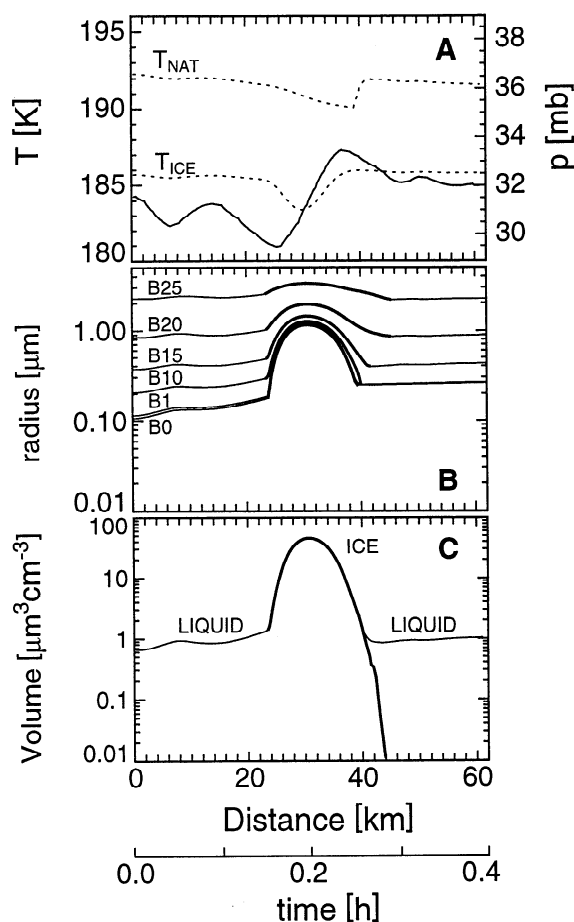


Figure 1. Microphysical box model simulations of the PSC event in Plate 2. (a) Temperature; (b) particle radii (thin lines, liquid; thick line, ice); (c) particle volume. Cooling upwind of the ice cloud leads to uptake of HNO_3 and H_2O by the $\text{H}_2\text{SO}_4/\text{H}_2\text{O}$ droplets and an increase in droplet size shown in Figures 1b and 1c. All droplets were assumed to freeze as ice 4.1 K below the ice frost point, and were then allowed to grow as ice/liquid mixtures. Evaporation of ice upon warming again was assumed to lead to the release of liquid aerosols again. The ice and NAT equilibrium temperatures are plotted as dotted lines in Figure 1a.

transiently in equilibrium with the gas phase, which implies that the temperature must be below the frost point (calculated in terms of the total water vapor in the air parcel of 5 ppmv). How much point 1 is below the frost point depends on the amount of water vapor condensed as ice, which can be estimated from the microphysical model simulation. We calculate the actual temperature at point 1 to be 183.8 ± 0.5 K. Temperatures at other locations in the wave can then be calculated from this reference temperature by assuming dry adiabatic behavior.

The adiabatic cooling and heating rates experienced by the air parcels are extremely high. For example, between 30 and 40 km the air descends about 800 m in 6 min, equivalent to an adiabatic heating rate of 80 K h^{-1} , which is considerably greater than typical synoptic temperature changes of 2 K h^{-1} . These rapid

temperature changes mean that even the ice particles are strongly out of equilibrium; note that the maximum in the backscatter ratio (Plate 2a) and ice particle volume (Figure 1c) occur during the warming phase of the wave. This is true for all strongly depolarizing clouds in Plates 2 and 5, with the exception of the cloud at ≈ 15 km horizontal distance in Plate 2. This very thin cloud is hardly visible in the total backscatter, and S_{\perp} reaches a maximum in the cooling phase of the wave without any apparent supercooling requirement. The origin of this cloud is not clear, but it is likely that the solid particles originated from processes upstream of flight leg 5. In the following analysis, we choose a trajectory more than 1 km lower in altitude which originates in a region without any indication of preexisting solid particles ($S_{\perp} \approx 1$)

2.1.1. Supercooling of ternary droplets. In order to reproduce the observed location and duration of the ice cloud in the microphysical simulation it was necessary to apply a cooling of 4.1 K below the ice frost point before the ice particles nucleated. This estimate is probably uncertain to within about ± 0.5 K due to uncertainties in the location of the ice frost point, as described above. However, it should be stressed that a cooling of at least 3 K can be read off directly from the measured backscatter, without reference to microphysical modeling: The point of first ice occurrence in Plate 2a (point 2) lies about 280 m above the point of maximum backscatter (point 1), which is equivalent to 2.8 K of cooling under dry adiabatic conditions. Clearly, because point 1 is known to be below the frost point, temperatures must have been at least 2.8 K below the ice frost point when ice formed at point 2. Note that due to the very rapid initial growth of ice from supercooled droplets, the point where ice particles became visible is very close to where the droplets froze.

This estimate of ≈ 3 –4 K cooling below the ice frost point is equivalent to a supercooling of the ternary $\text{HNO}_3/\text{H}_2\text{SO}_4/\text{H}_2\text{O}$ solution droplets below the ice melting point of between 58 and 65 K. This is much greater than the ≈ 35 K supercooling of $\text{H}_2\text{SO}_4/\text{H}_2\text{O}$ droplets observed in laboratory experiments [Bertram *et al.*, 1996] and estimated from nucleation rate calculations [Jensen *et al.*, 1991], and somewhat higher than the 30–60 K supercooling observed for ternary solutions droplets [Molina *et al.*, 1997]. Our estimate of 4 K cooling below the frost point is also larger than the recent calculations of Tabazadeh *et al.* [1997] for aqueous HNO_3 – H_2O droplets.

2.1.2. Ice particle number densities. These quasi-Lagrangian observations can also be used to constrain the number of ice crystals that nucleated. Changing the ice number density causes a change in the ice particle size distribution and hence the optical properties of the cloud. The approximate number of ice particles can therefore be determined by matching the calculated backscatter ratio in both polarizations and at both laser wavelengths with the observations, while

adjusting the assumed ice number density in the microphysical model.

The color ratio is a particularly sensitive measure of the particle size since the amount of backscattered light depends on the ratio of the lidar wavelength to particle radius. It shows a minimum of about 1 where the backscatter ratio is highest, but a maximum of up to 4 where the ice cloud is growing or dissipating (Plates 2c and 2d). Plate 3 shows the calculated color ratio as a function of ice particle size and shape compared with two ice particle size distributions at times corresponding to the first peak in color ratio and the subsequent minimum. Note that the colors used to indicate the magnitude of the color ratio are the same as in Plates 2 and 5. Clearly, the two maxima are caused by the ice particle radius passing through the region of enhanced color ratio for radii between about 0.5 and 0.9 μm . The ability to model such detailed features supports the assumption that the white line in Plates 2a, 2c and 2e represents an air parcel trajectory. Further calculations reveal that the occurrence of these peaks depends sensitively on the size distribution of liquid aerosols prior to freezing, which probably explains why such peaks did not appear in the two clouds immediately above the main cloud (note, however, that they are again visible in Plate 5c). It is also clear from Plate 3 that such peaks in color ratio occur only for aspect ratios $0.85 < \epsilon < 1.2$, indicating that the ice particles are rather close to spherical.

Matching of the three calculated and observed optical properties indicates that freezing occurred in at least 50% of the droplets, and most likely in most of them. In Plate 2 we show the case with complete ice activation. Such efficient ice activation, corresponding to ice particle number densities of greater than 5 cm^{-3} , is consistent with earlier in situ observations of meso-scale PSCs [Deshler *et al.*, 1994] but is considerably higher than the $0.001\text{--}0.01 \text{ cm}^{-3}$ typically observed in synoptic-scale PSCs [Dye *et al.*, 1992]. Such high ice particle number densities in mountain waves have also been predicted from nucleation theory by Tabazadeh *et al.* [1997]. They suggest that the difference between number densities in mountain waves and on the synoptic scale is most likely related to the cooling rate, and hence the supercooling that can be maintained during ice growth, rather than the different compositions of liquid aerosols in the two cases. Further experiments would be required to confirm this.

2.2. Sensitivity tests

Plate 4 highlights the sensitivity of the optical calculations to three variable quantities in the microphysical model: the cooling below the frost point required for ice formation, the number of ice particles nucleated, and the effect of possible nitric acid hydrate formation.

Cases 1–4 in Plate 4a show the calculated backscatter ratio for different ice supercooling assumptions of 0, 2, 3

and 3.5 K, while case 0 shows the calculation with 4.1 K as in Plate 2. Clearly, the horizontal extent of the ice cloud is highly dependent on the degree of supercooling assumed. Within the uncertainty of the air parcel temperature of $\pm 0.5 \text{ K}$, our estimated 4.1 K cooling below the frost point before ice formation (case 0) is robust. Cases 5 and 6 show the calculated backscatter for two different ice number densities corresponding to 50 and 30% of the total number of initial droplets. In this simulation the supercooling requirement was set to 4.1 K as in Plate 2. Reducing the number of freezing droplets leads to a fewer number of ice particles (which therefore have a larger radius) and a lower total ice mass at the peak in volume. This yields a lower backscatter ratio in poor agreement with the observations.

The magnitude of S_{\perp} upwind and downwind of the main ice cloud in Plate 2 is low, not indicating any nitric acid hydrate formation. Plate 4b shows a sensitivity calculation in which NAT was assumed to form heterogeneously on the ice particles. The three dashed lines represent different degrees of NAT nucleation. In each case, NAT was assumed to form on the small ice/liquid particles, as discussed in the next section, and the percentages refer to the number of particles that nucleated NAT. When a larger number of ice particles serve as sites for NAT nucleation, the NAT growth is faster due to the greater surface area available for condensational growth. We estimate that if NAT had been present downwind of the ice cloud, then the number density must have been less than 1 cm^{-3} (10% activation) for S_{\perp} to be indistinguishable from the signal noise, as observed. With such low number densities, the subsequent NAT particle growth would have been so slow as to become apparent only much farther downwind. However, hydrate formation on the ice cannot be excluded from these observations because the aircraft changed direc-

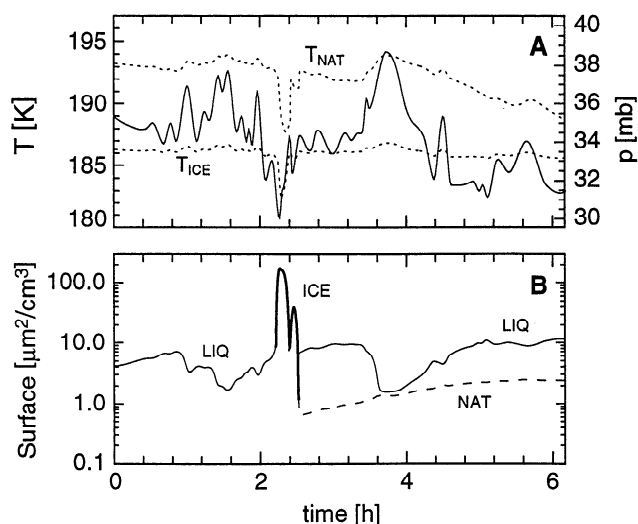


Figure 2. Microphysical box model calculations for the PSC shown in Plate 5. (a) Temperature; (b) particle surface area. The parameters of the microphysical model are as in Figure 1.

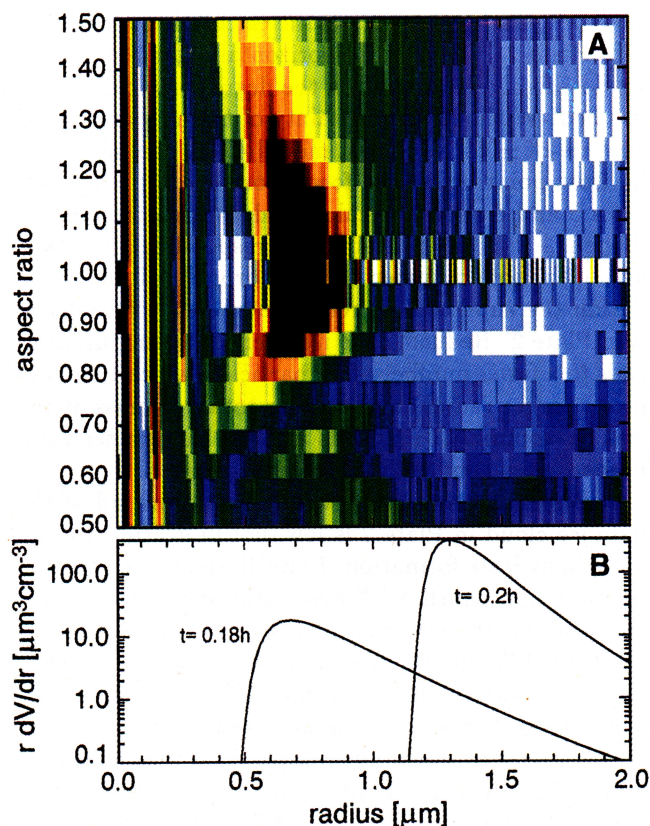


Plate 3. (a) The color ratio $(\beta_{\text{aerosol}}^{354\text{nm}} / \beta_{\text{aerosol}}^{532\text{nm}})$ for ice particles as a function of particle aspect ratio (ϵ) and radius; (b) ice particle volume distributions at 0.18 and 0.20 hours in Plate 2. The parameter $\epsilon = 1$ indicates spherical particles, $\epsilon < 1$ indicates prolate, and $\epsilon > 1$ is prolate spheroids. Each grid square in Plate 3a indicates the calculated color ratio for particles of the single radius and aspect ratio indicated. The color scale in Plate 3a is the same as in Plates 2c and 5c. Calculations were made using a T matrix light scattering algorithm [Mishchenko, 1991] with a refractive index of ice of 1.31 at 532 nm.

tion after reaching the right-hand side of Plate 2. We now describe a case where hydrate nucleation is apparent.

3. Ice-Induced Hydrate Formation

Plate 5 shows results from leg 3. In contrast to the case shown in Plate 2, these observations follow the development of the aerosol particles over an extended range downstream of the ice cloud, showing the emergence of a “tail” of strongly depolarizing solid particles that grow as the air cools again. These solid particles were also apparent in the lee of the mountains along flight leg 1 and as a uniform layer centred at 23 km altitude along leg 4. This contrasts with the observation of purely liquid aerosols upwind of the mountains along legs 1, 2 and 3. There is no discernable signal in the perpendicular channel on the upwind side of the ice cloud (at 250 km), indicating that the ice particles probably formed directly from the liquid droplets.

The shear between the direction of the aircraft in Plate 5 and the wind at the level of the PSC was approximately 30° . In order to model this PSC in a similar way to that in Plate 2 it is therefore necessary to assume that the cloud was uniform parallel to the ridge. Two further flight legs (2 and 4 in Plate 1) which showed practically uniform cloud decks suggest that this was probably the case. Also, as we show later, uniformity of the gross mesoscale temperature field is to be expected parallel to the Norwegian ridge. We note, however, that any interpretation of PSC development in this case will be less certain than for the quasi-Lagrangian PSC observations shown in Plate 2. The white line in Plates 5a, 5c and 5e represents the approximate trajectory of an air parcel flowing through the PSC, calculated by following the aerosol layers. A microphysical simulation was performed using the calculated temperatures (Figure 2a)

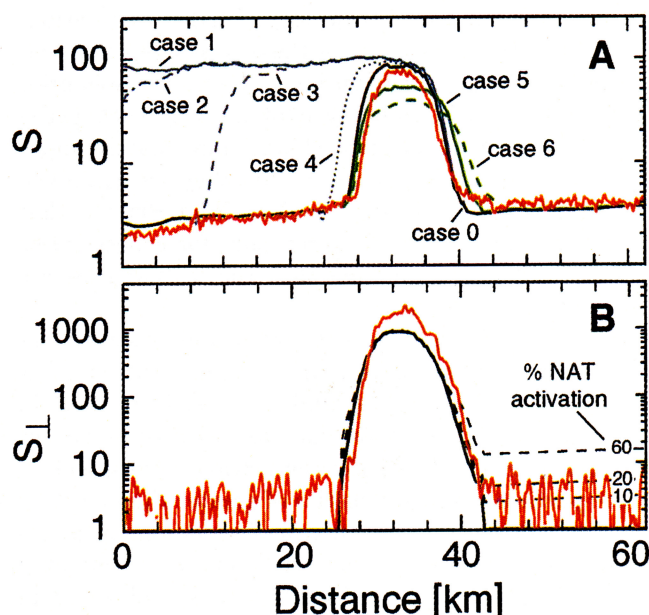


Plate 4. Sensitivity of calculated PSC optical properties to various quantities in the microphysical model simulation. An aspect ratio of 0.95 was assumed for ice particles and 0.85 for NAT. (a) Sensitivity of the backscatter ratio to changes in ice supercooling and ice number density. Red line, measured S along white line in Plate 2; case 0, assuming ice forms at $T_{\text{ice}} - 4.1$ K (as in Plate 2); case 1, assuming ice forms at T_{ice} ; case 2, assuming ice forms at $T_{\text{ice}} - 2$ K; case 3, assuming ice forms at $T_{\text{ice}} - 3$ K; case 4, assuming ice forms at $T_{\text{ice}} - 3.5$ K; case 5, assuming ice forms at $T_{\text{ice}} - 4.1$ K, but with 50% of the droplets activated to ice; case 6, assuming ice forms at $T_{\text{ice}} - 4.1$ K, but with 30% of the droplets activated to ice. (b) Sensitivity of S_\perp to NAT nucleation on ice particles. The percentages indicate the fraction of ice particles assumed to serve as sites for heterogeneous NAT nucleation. In each case the small ice particles are assumed to nucleate NAT, as discussed in the text. Hence 50% would indicate NAT formation on all ice/liquid particles smaller than the instantaneous number mode radius.

along this line and the results were used to calculate the optical properties shown in Plates 5b, 5d and 5f. As before, the number of ice particles was adjusted in order to gain agreement between the calculated optical properties and the lidar signal. As in the shorter wave

shown in Plate 2, the optical properties of the ice cloud are consistent with freezing of essentially all the liquid aerosols. The supercooling of the liquid aerosols before freezing was again set to 4.1 K below the ice frost point, yielding excellent agreement between the calculated optical properties and the lidar observations.

The solid particles downwind of the mountains are most likely composed of nitric acid hydrates, and could either have formed heterogeneously on the ice particles or in the highly nonequilibrium liquid droplets that develop during liquid PSC evaporation, as suggested by *Tsias et al.* [1997]. They showed that heating rates of 150 K h^{-1} could cause ternary $\text{HNO}_3/\text{H}_2\text{SO}_4/\text{H}_2\text{O}$ droplets to assume quasi-binary $\text{HNO}_3/\text{H}_2\text{O}$ compositions with an $\text{HNO}_3:\text{H}_2\text{O}$ molar ratio of 1:2.5. Such droplets were shown in aerosol chamber experiments to freeze homogeneously to nitric acid dihydrate (NAD). Heating rates as high as 135 K h^{-1} are evident in Plate 5. However, test calculations revealed that the number of nucleated NAD particles was extremely small, leading to solid particle growth much slower than required to explain any hydrate particles in these observations. We therefore consider the heterogeneous nucleation of a nitric acid hydrate (either NAD or NAT) on ice to be a more likely explanation for the solid particles in this case.

The number and size of hydrate particles in the tail can be estimated by comparing the observations with the combined results of the microphysical and optical calculations. Assuming the particles to be composed of NAT, best agreement between the three observed optical properties and the lidar simulation was obtained by assuming that only the smallest 2% of the ice particles served as sites for NAT nucleation. This is in agreement with the results of the sensitivity calculation shown in Plate 4b where only an upper limit to the number of NAT particles could be estimated. These particles grow to final radii of $\sim 0.8 \mu\text{m}$ at 800 km, leading to a gradual increase in S (Plate 5b) and S_{\perp} (Plate 5f), but a decrease in the color ratio (Plate 5d) in accord with the observations. We cannot identify unambiguously a physical reason for the number of NAT particles that were nucleated. One plausible explanation is related to the relative rates of deposition nucleation (gas to solid) and freezing nucleation. The microphysical calculations indicate that those ice particles that remained enclosed

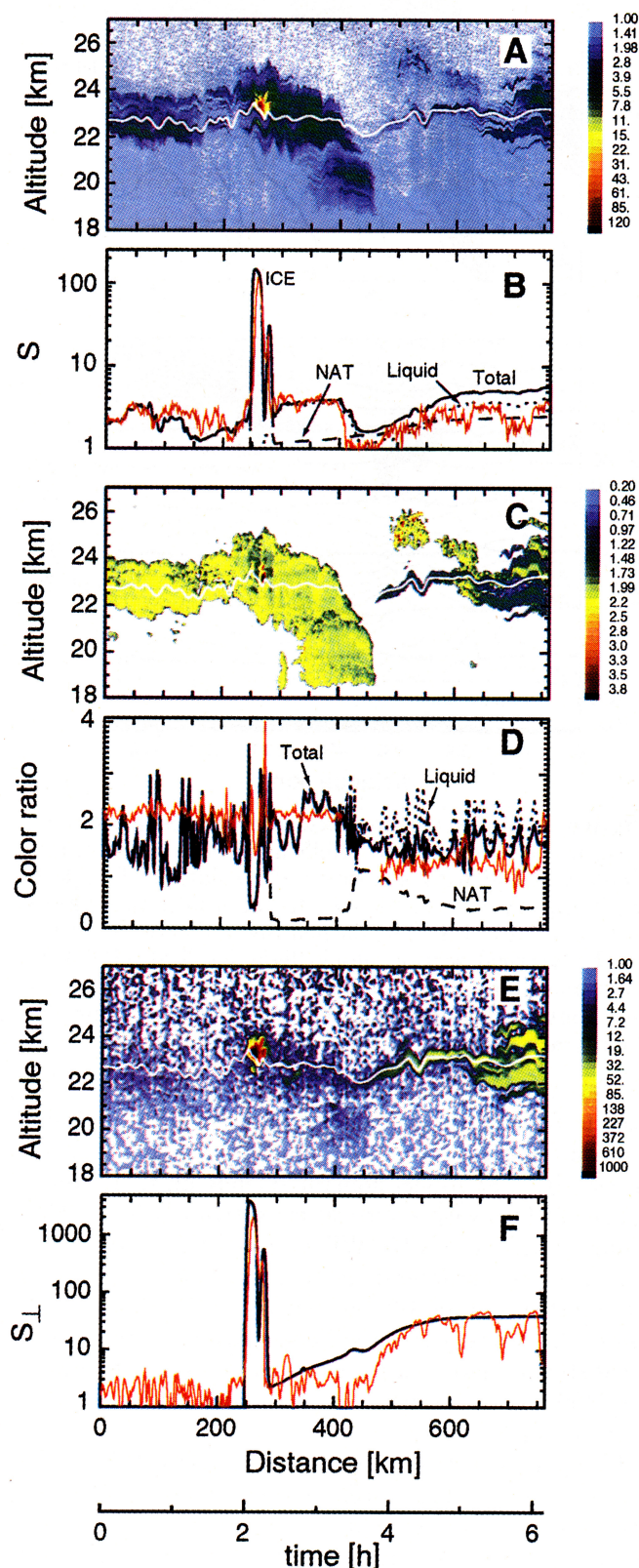


Plate 5. Lidar measurements of January 15, 1995 along flight leg 3. See Plate 2 for details. Nucleation of NAT was assumed to occur in the ice cloud (visible at 250 km) on ice particles belonging to bins 0 to 8 (the smallest 2% of the particles), leading to release of NAT upon ice evaporation. The remaining 98% of ice particles were assumed to release liquid droplets after ice evaporation. The contributions to the calculated lidar signal of liquid, NAT, and ice particles are shown in Plates 5b and 5d. The color ratios for liquid and NAT are defined as $\beta_{\text{liq}}^{354\text{nm}}/\beta_{\text{liq}}^{532\text{nm}}$ and $\beta_{\text{NAT}}^{354\text{nm}}/\beta_{\text{NAT}}^{532\text{nm}}$, respectively.

within a droplet did not form NAT, while those that grew large enough to become exposed to the gas phase did. This would be consistent with laboratory experiments indicating very slow nucleation of NAT out of a solution containing ice [Koop *et al.*, 1995; 1997b], but more rapid nucleation on an exposed ice crystal [Hanson, 1992]. Although plausible, verification of this mechanism requires in situ measurements.

It is not possible from these observations to distinguish between NAD or NAT activation. The principle differences between these two particles are the crystal density (and therefore particle size) and the temperature range over which they are thermodynamically stable (the NAD equilibrium temperature is about 1.6 K lower than the NAT equilibrium temperature). The difference in particle size cannot be distinguished due to the uncertainty in particle aspect ratio, while the different condensation or evaporation temperatures are difficult to distinguish due to the uncertainty in the air parcel trajectory in the particle tail.

Although a comprehensive microphysical interpretation of the PSC in Plate 5 is difficult, it nonetheless appears that localized cooling induced by air flow over the mountains was responsible for the formation of ice clouds. Furthermore, the observations are consistent with the mountain wave-induced formation of solid type 1 PSC particles that appeared downstream of the mountains. It seems likely that these formed heterogeneously on the ice PSCs. As we show below, mountain wave events of a similar magnitude to those in Plates 2 and 5 are quite common, implying that the phase of PSCs observed on the synoptic scale could be frequently influenced by events occurring on the mesoscale. However, the likely effect of mountain waves on the phase of stratospheric aerosols highlighted here still leaves open that other aerosol freezing mechanisms can occur on the synoptic scale, as suggested by Tabazadeh *et al.* [1996].

4. Mesoscale Dynamics

The ECMWF synoptic temperatures shown in Plate 1 are more than 10 K too warm to explain the formation of the observed PSCs. Thus the PSCs in Plates 2 and 5 appear to be caused by the effect of mesoscale meteorological disturbances, such as gravity waves over the Norwegian mountains. Conditions during this period were favorable for the generation of gravity waves since the low-level wind was strong and had a distinct cross-ridge component with no significant directional shear up to stratospheric levels. To confirm the role of gravity waves, the nonhydrostatic version of the NCAR/PSU mesoscale model MM5 [Dudhia, 1993; Grell *et al.*, 1994] was used to calculate the mountain wave-induced stratospheric temperature fluctuations on January 15, 1995.

The MM5 model region used here consists of a coarse domain with 36 km horizontal resolution covering Scandinavia entirely. Interactive grid nesting can then be

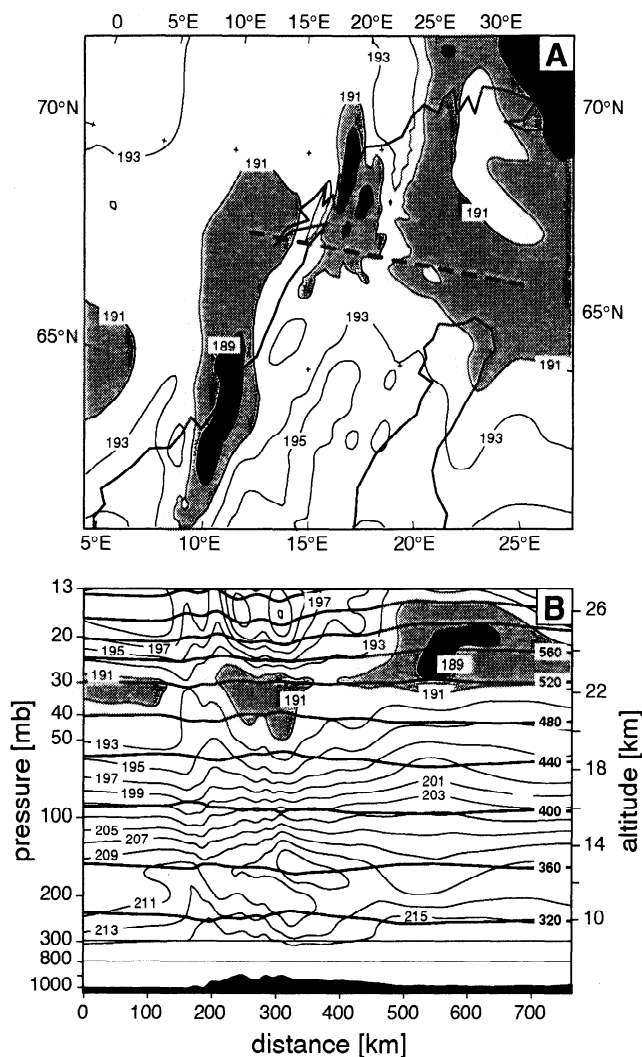


Figure 3. Mesoscale simulations of stratospheric temperature for January 15, 1995 using the MM5 model [Dudhia, 1993] with a horizontal resolution of 12 km. (a) Temperatures on the 520 K potential temperature surface at 1100 UT. The dashed line indicates flight leg 3. (b) Vertical section along flight leg 3 at 1100 UT. Thin lines, temperature; thick lines, potential temperature (both in kelvins). The model orography along the flight track is shown at the bottom of Figure 3b.

used to achieve a higher resolution over northern Scandinavia, with two nests of 12 and 4 km resolution, respectively. The model domain extends up to 10 mbar (about 28 km) with a vertical resolution of 540 m. The model is driven by ECMWF-analyzed winds and temperatures at the lateral boundaries. The integration was started at 1200 UT on January 14, 1995, approximately 24 hours before the lidar measurements. Simulated stratospheric temperatures are shown in Figure 3 for 1100 UT on January 15, calculated with a 12 km horizontal resolution.

Comparison between the modeled mesoscale temperatures along flight leg 3 (dashed line in Figure 3a) and the corresponding lidar image in Plate 5 reveals remarkable structural agreement between the enhanced

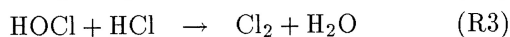
backscatter ratio and regions below 191 K. However, there is a significant difference between the minimum modeled temperatures of ~ 189 K and those inferred from the lidar observations via microphysical arguments, which are closer to 181 K. Certainly, the horizontal scale of the observed ice PSC (less than 20 km) is too small to be resolved by the mesoscale model; the horizontal short wavelength limit of vertically propagating gravity waves in the atmosphere is given approximately by $2\pi U/N$, where U is the horizontal wind speed and N is the Brunt-Vaisala frequency, given by $N^2 = (g/T)(dT/dz + \Gamma)$, where dT/dz is the local vertical temperature gradient, g is the acceleration due to gravity, and Γ is the adiabatic lapse rate. This implies a short wavelength limit of about 10 km, which would require a model horizontal resolution better than 1 km. Thus it is to be expected that the real temperature fluctuations exceed the model temperature fluctuations.

Further simulations with a 4 km horizontal resolution yielded small patches of cold air with temperatures below 189 K and a minimum temperature of about 186 K in the central cold region. Particularly important for the interpretation of the PSCs described here is that the gross scale temperature field shown in Figure 3 persisted for several hours, thus supporting our assumption that the PSCs in this region were quasi-stationary.

The simulated stratospheric temperatures also agree well with radiosonde data available for this region. Comparing the modeled temperatures (in parentheses) with the sounding from Orland indicates the good agreement: 186.9 K (188.3 K), 190.7 K (189.4 K), and 197.7 K (198.6 K) at 20, 30 and 50 mbar, respectively. Also at Bodø, Luleå, and Sodankylä the modeled temperatures deviate from the observations by less than 3 K. Discrepancies could be caused by small-scale waves or the uncertainty in the horizontal balloon location due to downstream drift, which was not taken into account in these comparisons.

5. Implications for Ozone Depletion

The very low temperatures together with the large particle surface areas that developed in this mountain wave PSC mean that the rates of important heterogeneous reactions must have increased dramatically. The most important surface-catalyzed reactions that can cause the activation of the dominant chlorine reservoir gases ClONO_2 and HCl are



The rate coefficients of these reactions increase sharply with decreasing temperature on liquid and NAT particles [DeMore *et al.*, 1997], making them much more effective during localized cooling events compared with the synoptic temperatures suggested in Plate 1. In ad-

dition, the increase in particle surface area in the ice PSC over that expected under synoptic conditions (Figure 2b) is greater than the accompanying increase in the rate coefficients. In combination, these two effects lead to an increase in the heterogeneous processing rate due to reaction (R1) by more than a factor of 500 in the ice cloud compared with synoptic conditions in this region.

Carslaw *et al.* [1998] show chemical box model calculations for the small PSC in Plate 2. These calculations reveal that even such a small-scale wave can lead to heterogeneous activation of almost half of the available inorganic chlorine. Such a rapid conversion of chlorine reservoir gases to reactive forms is particularly remarkable considering that the air spends only a few minutes in the wave.

The extent of chlorine activation and the subsequent effect on ozone depletion resulting from this mechanism depends critically on the frequency with which such mountain waves occur. Plate 6 shows the distribution of localized mountain-induced air parcel displacements on the 30 mbar level for January 15, 1995, calculated using a mountain wave forecast model [Bacmeister *et al.*, 1994]. Calculated vertical displacements over northern Norway are between 1000 and 2000 m, equivalent to a 10–20 K change in temperature, which is in reason-

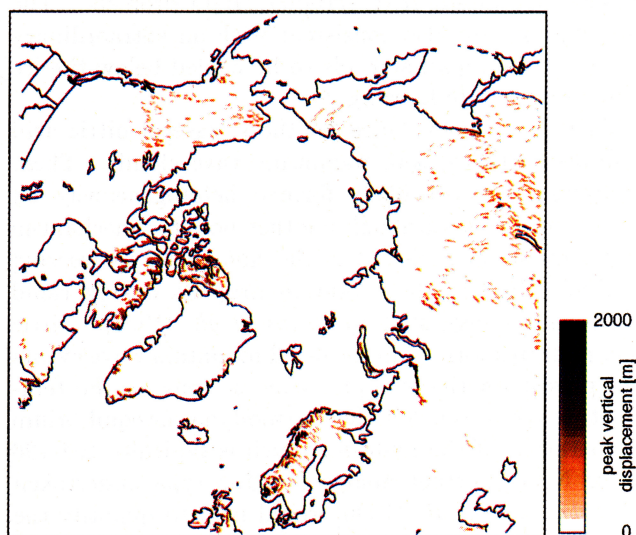


Plate 6. Peak vertical displacements of air parcels flowing over mountain ranges in the Arctic on January 15, 1995. Results are shown for the 30 mbar level. Each 1000 m of vertical displacement corresponds to ~ 10 K temperature perturbation from the mean value. The mountain wave forecast model [Bacmeister *et al.*, 1994] uses a global database of topographic features containing estimates of height, width, and orientation. A simple 2-D hydrostatic wave model is forced above each feature with $5^\circ \times 2^\circ$ global analyses of wind and temperature from the National Center for Environmental Prediction. Symbols indicate location, approximate size, and orientation of topographic features. Symbol color indicates peak amplitude of 2-D hydrostatic waves forced over a given topographic feature.

able agreement with the observed 12–13 K cooling indicated by comparing temperatures in Plate 1 and Figure 2. Simplifying assumptions in the mountain wave forecast model may sometimes lead to overestimates of peak wave amplitudes, while at the same time underestimating the horizontal extent of individual mountain wave events.

In the work of *Carshaw et al.* [1998] we have examined the rate at which air is processed through these mountain waves over an entire Arctic winter and how this can affect chlorine activation and ozone depletion on the scale of the Arctic vortex. The results indicate that the occurrence of strong mountain waves may be sufficiently frequent to significantly increase the chlorine activation due to synoptic scale PSCs.

6. Discussion

Quasi-Lagrangian observations of stationary PSCs over the Norwegian mountains provide a unique opportunity to understand microphysical and chemical processes occurring in such clouds. We have shown that detailed information on aerosol freezing can be obtained by combining optical and microphysical models of the lidar signal. The observed water ice PSCs appear to have formed from almost complete activation of the background liquid $\text{HNO}_3/\text{H}_2\text{SO}_4/\text{H}_2\text{O}$ droplets. The observations are also consistent with an extraordinary ability of the liquid aerosols to be cooled below the ice frost point before freezing.

There is clear evidence for the release of nitric acid hydrate particles from mountain wave clouds. These particles are most likely formed heterogeneously on the ice particles, although another possible mechanism that cannot be excluded is the homogeneous freezing of $\text{HNO}_3/\text{H}_2\text{SO}_4/\text{H}_2\text{O}$ solution droplets during rapid warming, as suggested by *Tsias et al.* [1997]. Nitric acid hydrates formed in localized mountain wave events will persist on the synoptic scale so long as the temperature remains below the thermodynamic equilibrium temperature of the hydrate, which is typically 194–196 K for NAT. Further analyses of the type undertaken by *Tabazadeh et al.* [1996] would help to quantify the global significance of such PSC formation. An estimate of the contribution of mountain waves to solid PSCs on the scale of the polar vortex and for an entire winter would also be useful. Preliminary studies undertaken by us reveal that the greatest predominance of NAT clouds caused by this mechanism are likely to occur downwind of the Norwegian mountains and the Urals in Russia.

Our simulations show that the nucleation of NAT particles in mountain waves may often be a highly selective process, yielding a small number of large particles with a potentially significant fall velocity. Large-scale NAT activation by this mechanism could therefore contribute to denitrification at the altitude of cloud formation, and renitrification at lower altitudes, as has been clearly ob-

served in recent years in the Arctic [e.g., *Fischer et al.*, 1997].

Carshaw et al. [1998] have shown that mountain waves can be encountered frequently by air parcels confined within the Arctic polar vortex. The extent to which mountain waves contribute to ozone depletion in the Arctic needs to be assessed through a combination of field measurements of individual events and large-scale modeling studies. Mountain wave clouds such as described here provide a very good natural laboratory in which to study processes such as chlorine activation since the clouds remain stationary for relatively long periods of time. An ideal experiment would be to measure simultaneously the PSC by lidar and the key chlorine species upwind and downwind.

Field studies and analyses of existing measurements are urgently needed in order to better quantify the temperature changes that occur over different mountain ranges. A knowledge of the temperature in such waves is critical because of the sharp increase in heterogeneous processing rates with decreasing temperature. Because of the need to predict mountain waves on a global scale, it will be necessary to examine not only individual wave events, but also satellite measurements of temperature fluctuations and mountain wave clouds where these occur. Gravity wave sources other than mountains should also be examined for their potential role in PSC production and chlorine activation. *Wu and Waters* [1996a, b] have shown from Microwave Limb Sounder satellite measurements that stratospheric gravity waves can be associated also with strong tropospheric convection and stratospheric jetstreams well away from significant surface topography. *Fritts and Nastrom* [1992] have also studied mesoscale variability due to frontal activity, nonfrontal convection, and wind shear. These data were obtained aboard commercial aircraft during the Global Atmospheric Sampling Program (GASP) in 1978 and 1979 and from the corresponding meteorological analyses and satellite imagery. At present there exists no observational climatology of the magnitude or frequency of occurrence of these gravity wave events, making it difficult to assess their importance to stratospheric chemistry and particle microphysics.

Acknowledgments. The help of M. Mishchenko (NASA Goddard, New York) with the T matrix calculations is gratefully acknowledged. Financial support for A. Tsias is gratefully acknowledged from the Bundesministerium für Bildung, Wissenschaft, Forschung und Technologie under contract 01 LO 9506/0, for K. S. Carshaw from the European Communities under contract ENVCT95-0050 and DG XII, and for J. T. Bacmeister from The Office of Naval Research (ONR) and NASA's Atmospheric Chemistry Modeling and Analysis Program (ACMAP).

References

- Bacmeister, J.T., P.A. Newman, B.L. Gary and K.R. Chan, An algorithm for forecasting mountain wave-related tur-

- bulence in the stratosphere, *Weather and Forecasting*, **9**, 241, 1994.
- Bertram, A.K., D.D. Paterson, and J.J. Sloan, Mechanisms and temperatures for the freezing of sulfuric acid aerosols measured by FTIR extinction spectroscopy, *J. Phys. Chem.*, **100**, 2376-2383, 1996.
- Borrmann, S., S. Solomon, J.E. Dye, D. Baumgardner, K.K. Kelly, and K.R. Chan, Heterogeneous reactions on stratospheric background aerosols, volcanic sulfuric acid droplets, and type 1 polar stratospheric clouds: Effects of temperature fluctuations and differences in particle phase, *J. Geophys. Res.*, **102**, 3639-3648, 1997.
- Carslaw, K.S., B.P. Luo, S.L. Clegg, T. Peter, P. Brimblecombe, and P. Crutzen, Stratospheric aerosol growth and HNO_3 gas phase depletion from coupled HNO_3 and water uptake by liquid particles, *Geophys. Res. Lett.*, **21**, 2479-2482, 1994.
- Carslaw, K.S., T. Peter and S.L. Clegg, Modeling the composition of liquid stratospheric aerosols, *Rev. Geophys.*, **35**, 125-154, 1997.
- Carslaw, K.S., et al., Increased stratospheric ozone depletion due to mountain-induced atmospheric waves, *Nature*, in press, 1998.
- DeMore, W., et al., Chemical Kinetics and Photochemical Data for Use in Stratospheric Modeling, JPL Publication 97-4, 1997.
- Deshler, T., T. Peter, R. Müller, and P.J. Crutzen, The lifetime of leewave-induced ice particles in the Arctic stratosphere: 1. Balloonborne observations, *Geophys. Res. Lett.*, **21**, 1327-1330, 1994.
- Dörnbrack, A., M. Leutbecher, H. Volkert, and M. Wirth, Mesoscale forecasts of stratospheric mountain waves, *Meteorol. Appl.*, in press, 1997.
- Drdla, K., et al., Analysis of the physical state of one Arctic polar stratospheric cloud based on observations, *Geophys. Res. Lett.*, **21**, 2473-2478, 1994.
- Dudhia, J., A non-hydrostatic version of the Penn State-NCAR Mesoscale Model: Validation tests and simulation of an Atlantic cyclone and cold front, *Mon. Weather Rev.*, **121**, 1493, 1993.
- Dye, J.E., et al., Particle size distributions in Arctic polar stratospheric clouds, growth and freezing of sulfuric acid droplets, and implications for cloud formation, *J. Geophys. Res.*, **97**, 8015-8034, 1992.
- Fritts, D.C., and G.D. Nastrom, Sources of mesoscale variability of gravity-waves, 2, frontal, convective, and jet-stream excitation, *J. Atmos. Sci.*, **49**, 111-127, 1992.
- Fischer, H., et al., Observations of high concentrations of total reactive nitrogen (NO_y) and nitric acid in the lower Arctic stratosphere during the STREAM II campaign in February 1995, *J. Geophys. Res.*, **102**, 23,559-23,571, 1997.
- Gary, B.L., Observational results using the microwave temperature profiler during the Airborne Antarctic Ozone Experiment, *J. Geophys. Res.*, **94**, 11,223-11,231, 1989.
- Grell, G.A., J. Dudhia, and D.R. Stauffer, A description of the fifth-generation Penn State/NCAR mesoscale model (MM5), *Tech. Note 398*, 121 pp., Nat. Cent. for Atmos. Res., Boulder, Colo., 1994.
- Hanson, D.R., The uptake of HNO_3 onto ice, NAT, and frozen sulfuric acid, *Geophys. Res. Lett.*, **19**, 2063-2066, 1992.
- Hanson, D., and K. Mauersberger, Laboratory studies of the nitric acid trihydrate: Implications for the south polar stratosphere, *Geophys. Res. Lett.*, **15**, 855-858, 1988.
- Jensen, E.J., O.B. Toon, and P. Hamill, Homogeneous freezing nucleation of stratospheric solution droplets, *Geophys. Res. Lett.*, **18**, 1857-1860, 1991.
- Koop, T., B.P. Luo, U.M. Biermann, P.J. Crutzen, and T. Peter, Do stratospheric aerosol droplets freeze above the ice frost point?, *Geophys. Res. Lett.*, **22**, 917-920, 1995.
- Koop, T., K.S. Carslaw, and T. Peter, Thermodynamic stability and phase transitions of PSC particles, *Geophys. Res. Lett.*, **24**, 2199-2202, 1997a.
- Koop, T., B.P. Luo, U.M. Biermann, P.J. Crutzen, and T. Peter, Freezing of $\text{HNO}_3/\text{H}_2\text{SO}_4/\text{H}_2\text{O}$ solutions at stratospheric temperatures: Nucleation statistics and experiments, *J. Phys. Chem.*, **101**, 1117-1133, 1997b.
- Krieger, U., B.P. Luo, J. Mössinger, U. Weers, and T. Peter, Refractive indices of $\text{H}_2\text{SO}_4/\text{HNO}_3/\text{H}_2\text{O}$ solutions to stratospheric temperatures, paper presented at the 1997 Conference on the Atmospheric Effects of Aviation, Virginia Beach, Va., 1997.
- Leutbecher, M., and H. Volkert, Stratospheric temperature anomalies and mountain waves: A three-dimensional simulation using a multi-scale weather prediction model, *Geophys. Res. Lett.*, **23**, 3329-3332, 1996.
- Meilinger, S.K., et al., Size-dependent stratospheric droplet composition in lee wave temperature fluctuations and their potential role in PSC freezing, *Geophys. Res. Lett.*, **22**, 3031-3034, 1995.
- Mishchenko, M.I., Light scattering by randomly oriented axially symmetric particles, *J. Opt. Soc. Am.*, **8**, 871-882, 1991.
- Molina, M.J., A.H.-Y. Chang, S.T. Martin, L.T. Molina, H. Ng, and D. Salcedo, Laboratory studies of the $\text{H}_2\text{SO}_4/\text{HNO}_3/\text{H}_2\text{O}$ system related to PSC formation mechanisms, Paper presented at the 1997 Conference on the Atmospheric Effects of Aviation, Virginia Beach, Va., 1997.
- Nastrom, G.D., and D.C. Fritts, Sources of mesoscale variability of gravity waves, I: Topographic excitation, *J. Atmos. Sci.*, **49**, 101-110, 1992.
- Peter, T., Microphysics and chemistry of polar stratospheric cloud particles, *An. Rev. Phys. Chem.*, **48**, 785-822, 1997.
- Peter, T., R. Müller, K. Drdla, K. Petzoldt, and E. Reimer, A microphysical box model for EASOE: Preliminary results for the January/February 1990 PSC event over Kiruna, *Ber. Bunsenges. Phys. Chem.*, **96**, 362-367, 1992.
- Peter, T., R. Müller, P.J. Crutzen and T. Deshler, The lifetime of leewave-induced ice particles in the Arctic stratosphere, 2, Stabilization due to NAT-coating, *Geophys. Res. Lett.*, **21**, 1331-1334, 1994.
- Tabazadeh, A., R.P. Turco, and M.Z. Jacobson, A model for studying the composition and chemical effects of stratospheric aerosols, *J. Geophys. Res.*, **99**, 12,897-12,914, 1994a.
- Tabazadeh, A., R.P. Turco, K. Drdla, M.Z. Jacobson, and O.B. Toon, A study of Type I polar stratospheric cloud formation, *Geophys. Res. Lett.*, **21**, 1619-1622, 1994b.
- Tabazadeh, A., O.B. Toon, B.L. Gary, J.T. Bacmeister, and M.R. Schoeberl, Observational constraints on the formation of Type 1a polar stratospheric clouds, *Geophys. Res. Lett.*, **23**, 2109-2112, 1996.
- Tabazadeh, A., O.B. Toon, and E.J. Jensen, Formation and implications of ice particle nucleation in the stratosphere, *Geophys. Res. Lett.*, **24**, 2007-2010, 1997.
- Tolbert, M.A., Stratospheric aerosols and polar stratospheric cloud formation, *Science*, **264**, 527, 1994.
- Toon, O.B., E.V. Browell, S. Kinne, and J. Jordan, An analysis of lidar observations of polar stratospheric clouds, *Geophys. Res. Lett.*, **17**, 393-396, 1990.
- Tsias, A., A. Prenni, K.S. Carslaw, T.P. Onasch, B.P. Luo, M.A. Tolbert, and T. Peter, Freezing of polar stratospheric clouds in orographically induced strong warming events, *Geophys. Res. Lett.*, **24**, 2303-2306, 1997.
- Volkert, H., and D. Intes, Orographically forced strato-

- spheric waves over northern Scandinavia, *Geophys. Res. Lett.*, **19**, 1205-1208, 1992.
- Wirth, M., and W. Renger, Evidence of large-scale ozone depletion within the Arctic polar vortex 1994/1995 based on airborne lidar measurements, *Geophys. Res. Lett.*, **23**, 813-816, 1996.
- World Meteorological Organisation, Scientific assessment of ozone depletion: 1994, *Rep. 37*, Geneva, 1994.
- Wu, D.L., and J.W. Waters, Gravity-wave-scale temperature fluctuations seen by the UARS Microwave Limb Sounder, *Geophys. Res. Lett.*, **23**, 3289-3292, 1996a.
- Wu, D.L., and J.W. Waters, Satellite observations of atmospheric variances: A possible indication of gravity waves, *Geophys. Res. Lett.*, **23**, 3631-3634, 1996b.
-
- J. Bacmeister, Code 7641, Naval Research Laboratory, Washington, D.C. 20375. (e-mail: julio@ismap5.nrl.navy.mil)
- K.S. Carslaw, B.P. Luo, T. Peter, and A. Tsias, Max-Planck-Institut für Chemie, Postfach 3060, Mainz 55020, Germany. (e-mail: carslaw@mpch-mainz.mpg.de; peter@nike.mpch-mainz.mpg.de; tsias@mpch-mainz.mpg.de)
- A Dörnbrack, M. Leutbecher, W. Renger, H. Volkert, and M. Wirth, Deutsche Forschungsanstalt für Luft- und Raumfahrt, 82230 Wessling, Germany. (e-mail: pa2o@atlas.op.dlr.de; M.Leutbecher@dlr.de; Wolfgang.Renger@dlr.de; Hans.Volkert@dlr.de; Martin.Wirth@dlr.de)

(Received July 11, 1997; revised October 20, 1997;
accepted November 30, 1997.)